JOURNAL OF GEOPHYSICAL RESEARCH, VOL. 114, A10106, doi:10.1029/2009JA014376, 2009

Low-frequency whistler waves and shocklets observed at quasi-perpendicular interplanetary shocks

L. B. Wilson III,[1] C. A. Cattell,[1] P. J. Kellogg,[1] K. Goetz,[1] K. Kersten,[1] J. C. Kasper,[2] A. Szabo,[3] and K. Meziane[4]

Received 21 April 2009; revised 23 June 2009; accepted 2 July 2009; published 17 October 2009.

[1] We present observations of low-frequency waves (0.25 Hz < f < 10 Hz) at five quasi-perpendicular interplanetary (IP) shocks observed by the Wind spacecraft. Four of the five IP shocks had oblique precursor whistler waves propagating at angles with respect to the magnetic field of 20°–50° and large propagation angles with respect to the shock normal; thus they do not appear to be phase standing. One event, the strongest in our study and likely supercritical, had low-frequency waves consistent with steepened magnetosonic waves called shocklets. The shocklets are seen in association with diffuse ion distributions. Both the shocklets and precursor whistlers are often seen simultaneously with anisotropic electron distributions unstable to the whistler heat flux instability. The IP shock with upstream shocklets showed much stronger electron heating across the shock ramp than the four events without upstream shocklets. These results may offer new insights into collisionless shock dissipation and wave-particle interactions in the solar wind.

Citation: Wilson, L. B., III, C. A. Cattell, P. J. Kellogg, K. Goetz, K. Kersten, J. C. Kasper, A. Szabo, and K. Meziane (2009), Low-frequency whistler waves and shocklets observed at quasi-perpendicular interplanetary shocks, *J. Geophys. Res.*, *114*, A10106, doi:10.1029/2009JA014376.

1. Introduction

[2] Irregular turbulence upstream of planetary bow shocks has been observed for over 30 years. The frequencies of this turbulence were often observed to fall in the range of the ion cyclotron frequency. Thus, the magnetic turbulence upstream of the Earth's bow shock was initially examined in association with ion particle data [*Paschmann et al.*, 1981]. Three ion populations, reflected, intermediate, and diffuse, are commonly found in the terrestrial foreshock. Reflected ions have a beam-like distribution with bulk speeds on the order of 1–5 times the solar wind speed and they predominantly occur near shocks with shock normal angles, θ_{Bn}, between 30°–75° [*Paschmann et al.*, 1981]. Intermediate ion distributions represent a transition between reflected and diffuse. They appear as a crescent-shaped distribution with centers of curvature near the solar wind velocity. Diffuse ion distributions are a highly non-thermal, relatively isotropic distribution extending up to the highest energies measured (~40 keV). Diffuse ions often show anisotropies with pitch angle distributions peaking at 90° [*Paschmann et al.*, 1981].

[3] *Fairfield* [1974] initially classified the magnetic turbulence into two categories: low frequency (0.01–0.05 Hz) and high frequency (0.5–4.0 Hz). *Hoppe and Russell* [1983] studied ultralow frequency (ULF) waves, associated with intermediate and diffuse ions, classifying them as mixtures of transverse Alfvénic and compressional magnetosonic modes with rest frame frequencies ~0.1 Ω_{cp} (~0.01 Hz in solar wind) and wavelengths ~6000 km. More recent studies with higher-resolution particle instruments have found that the ULF wave boundary of the foreshock coincides with an inner boundary of field-aligned ion beams [*Meziane et al.*, 2004]. By radiating energy away from the shock itself, both transverse Alfvénic and compressional magnetosonic modes allow a collisionless shock to communicate with the upstream plasma by preheating or decelerating the incoming plasma, thus altering the Rankine-Hugoniot conditions [*Scholer and Belcher*, 1971]. Though waves in this frequency regime upstream of collisionless shocks are thought to play an intrinsic role in particle acceleration, heating, and energy dissipation [*Hada et al.*, 1987; *Stasiewicz et al.*, 2003], we will focus on the waves associated with Fairfield's higher-frequency regime in this study.

[4] *Fairfield*'s [1974] initial higher-frequency category was subdivided into a lower-frequency, larger amplitude wave and a higher-frequency, smaller amplitude wave. Both modes were observed to have a left-hand (LH) polarization in the spacecraft (SC) frame, but a RH polarization in the plasma rest frame [*Hoppe et al.*, 1981, 1982]. The apparent reversal of polarization was due to Doppler effects as the waves, with phase velocities slower than the solar wind, were blown back over the spacecraft. The lower-frequency

[1]Department of Physics and Astronomy, University of Minnesota, Minneapolis, Minnesota, USA.
[2]Harvard-Smithsonian Center for Astrophysics, Harvard University, Cambridge, Massachusetts, USA.
[3]NASA Goddard Space Flight Center, Greenbelt, Maryland, USA.
[4]Physics Department, University of New Brunswick, Fredericton, New Brunswick, Canada.

0148-0227/09/2009JA014376$09.00

mode, first described by *Russell et al.* [1971], was initially referred to as a discrete wave packet. Later studies have called them shocklets [*Hoppe et al.*, 1981] or short large-amplitude magnetic structures (SLAMS) [*Schwartz et al.*, 1992]. *Hoppe et al.* [1981], using the ISEE 1 and 2 satellites, found the shocklets to be ULF magnetosonic waves occasionally associated with a leading magnetosonic whistler wave train. *Lucek et al.* [2002], using the four Cluster spacecraft, concluded that SLAMS have shorter scale lengths than shocklets and that the two structures had many similarities. *Omidi and Winske* [1990] used an electromagnetic hybrid code to show shocklets were a consequence of wave spreading due to dispersive effects. As the magnetosonic waves steepened, magnetosonic whistler waves grew just downstream of the steepened portions and began to propagate upstream away from the steepened edge of the magnetosonic waves. This led to the whistler wave train ahead of the steepened magnetic field structure. *Scholer* [1993], using an electromagnetic hybrid code, found that ULF waves excited by ion beams steepen as they convect into regions of diffuse ions. Thus, as the ULF waves steepen, they dispersively radiate a whistler wave. Two more recent 1-D PIC simulation studies focused on the evolution of SLAMS excited by diffuse ion distributions [*Scholer et al.*, 2003; *Tsubouchi and Lembège*, 2004]. Both studies found SLAMS to result from steepened ULF waves and the leading whistler train to result from the radiation of the dispersive waves by the steepened edge of the SLAMS. Thus, *Scholer* [1993], *Scholer et al.* [2003], and *Tsubouchi and Lembège* [2004] concluded that ULF waves, shocklets, and SLAMS are all the same entity at different stages in their evolution, consistent with the results of *Schwartz et al.* [1992].

[5] Shocklets are observed with and without a whistler wave train [*Hoppe et al.*, 1981; *Le et al.*, 1989]. Shocklets were observed upstream of planetary foreshocks [*Hoppe et al.*, 1981], cometary foreshocks [*Le et al.*, 1989], and one observation at a quasi-parallel ($\theta_{Bn} \sim 40°$) IP shock [*Lucek and Balogh*, 1997]. The shocklets were found to have rest frame frequencies of $0.1 < \omega/\Omega_{cp} < 40$ ($\sim$0.001–0.4 Hz in solar wind), wavelengths of 30 km $\leq \lambda \leq$ 2100 km and propagation angles of $\theta_{kB} \sim 20°–30°$ [*Russell et al.*, 1971; *Hoppe et al.*, 1981]. Planetary foreshock studies have shown shocklets to always occur in association with diffuse ion distributions [*Hoppe et al.*, 1981, 1982; *Hoppe and Russell*, 1983].

[6] The higher-frequency waves of Fairfield's high-frequency category have been studied and found to be whistler waves [*Fairfield*, 1974]. On the high end of this frequency range (0.5–4.0 Hz), a nearly monochromatic whistler wave was discovered by *Hoppe et al.* [1981] upstream of the bow shock in association with reflected ion beam distributions. *Hoppe et al.* [1982] showed that the rest frame frequencies were $20 < \omega/\Omega_{cp} < 100$ ($\sim$0.2–10 Hz in the solar wind), wavelengths of $\sim$100 km, and propagation angles with respect to the magnetic field $\theta_{kB} \sim 20°–45°$. Oblique whistler waves with f $\sim$1 Hz were analyzed by *Farris et al.* [1993] upstream of low β quasi-perpendicular bow shocks finding the waves to be consistent with the $\sim$1 Hz whistlers reported by *Russell et al.* [1971] and *Hoppe et al.* [1981, 1982].

[7] *Mellott and Greenstadt* [1984] examined precursor whistler waves at the quasi-perpendicular bow shock. They found two different types of precursor whistler waves, a phase standing whistler wave propagating parallel to the shock normal and another whistler propagating parallel to the magnetic field. In the SC frame, the precursors propagating parallel to the magnetic field had higher frequencies ($\sim$1 Hz) than the phase standing precursor whistlers ($\sim$0.1 Hz). It is important to note that the $\sim$1 Hz waves studied by *Hoppe et al.* [1982] had relatively large θ_{kB} values, while the precursors of *Mellott and Greenstadt* [1984] were propagating parallel to the magnetic field, thus $\theta_{kB} \sim 0°$. *Mellott and Greenstadt* [1984] proposed that the parallel propagating precursors were products of the phase standing precursors. The precursors propagating parallel to the shock normal (the phase standing precursors) were found to have higher rest frame frequencies than the precursors propagating parallel to the magnetic field. The difference was due to their propagation with respect to the magnetic field. The Doppler effects on the parallel propagating precursors were negligible because the magnetic field was primarily directed in Y-GSE direction, roughly perpendicular to the solar wind velocity. Both the parallel propagating and phase standing precursors are characterized by a high degree of RH polarization and nearly monochromatic frequency spectrum. A more recent study by *Farris et al.* [1993] found $\sim$1 Hz, parallel propagating whistler waves to be consistent with the observations of *Mellott and Greenstadt* [1984]. The phase standing precursors observed by *Farris et al.* [1993], however, had wavelengths greater than the shock scale sizes they were associated with and rest frame frequencies $\sim 10\ \Omega_{cp}$ ($\sim$0.1 Hz in solar wind).

[8] There are fewer observations of these types waves upstream of IP shocks. This may be due to the fact that IP shocks are unlikely to produce conditions conducive to the production of these waves due to their massive scales, larger radius of curvature at 1 AU, tendency to have a quasi-perpendicular geometry, and typically lower Mach numbers. Not only are quasi-perpendicular shocks less likely to produce the diffuse ion distributions thought to be necessary for shocklet generation and growth, they are not intrinsically unstable to reformation when subcritical [*Farris et al.*, 1993]. Both *Hada et al.* [1987] and *Omidi and Winske* [1990] suggested shocklet generation mechanisms which require conditions more likely to occur in the foreshocks of planetary or cometary bow shocks connected to the quasi-parallel section.

[9] Using multisatellite measurements upstream from quasi-perpendicular and quasi-parallel IP shocks, *Russell et al.* [1983] observed two distinct wave types, a whistler precursor near the ramp and a 30 s wave they called irregular turbulence farther upstream which had a nearly featureless frequency spectrum. *Tsurutani et al.* [1983], in a study of $\sim$100 quasi-parallel (defined by the authors as $\theta_{Bn} < 65°$) IP shocks, found low-frequency waves ($\sim$0.05 Hz) to propagate within 15° of the ambient magnetic field. *Lucek and Balogh* [1997] observed one shocklet upstream of a quasi-parallel IP shock ($\theta_{Bn} \sim 40°$). The shocklet was similar to bow shock observations but showed a dispersive and "bursty" nature and the amplitude did not decay

smoothly with distance from the steepened edge of the shocklet itself.

[10] In this paper we present observations of low-frequency (0.25 Hz < f < 10 Hz) magnetic fluctuations in and around five quasi-perpendicular IP shocks. The waves are shown to be mixtures of whistler and magnetosonic modes and are observed in association with electron distributions unstable to the whistler heat flux and/or anisotropy instabilities. In the discussion of our data, all the steepened magnetosonic waves will be called shocklets. In section 2 we describe the instrumentation/data used and the analysis techniques. In section 3.1 we discuss observations of 12 shocklets upstream of a quasi-perpendicular IP shock, examining 2 shocklets in detail. Examples of minimum variance analysis and comparison to electron distributions are presented. In section 3.2, we discuss the four typical IP shocks and their differences from the unusual event. Then we discuss the particle data observations in section 3.3. Finally, in section 4 we discuss the importance of these results and discuss future work.

2. Data Sets and Analysis

[11] Electron and ion particle distributions, high time resolution (HTR) magnetic field data, and electric field intensities were obtained from the Wind spacecraft in and around five IP shocks on the following dates: 3 April 1996, 8 April 1996, 24 October 1997, 10 December 1997, and 6 April 2000. The magnetic field instrument [*Lepping et al.*, 1995] is composed of dual triaxial fluxgate magnetometers. The HTR MFI data were sampled at two different rates: ~22 samples/s (for 3 April 1996, 8 April 1996, and 24 October 1997) and ~11 samples/s (10 December 1997 and 6 April 2000). The Wind WAVES thermal noise receiver (TNR) measures ~4–256 kHz electric fields in 5 logarithmically spaced frequency bands with a 7 $nV/\sqrt{Hz}$ sensitivity and total dynamic range in excess of 100 dB [*Bougeret et al.*, 1995].

[12] Electron and ion distributions were obtained from the Wind 3DP EESA and PESA particle detectors [*Lin et al.*, 1995]. The EESA instruments (High and Low) consist of two top hat symmetrical spherical section electrostatic analyzers with microchannel plate detectors. The Eesa Low (EL) instrument can measure electrons at 16 different energies from a few eV to a little more than a keV for a full 4π steradian once every spin period (~3 s) in burst mode (ELB or EHB). The Eesa High (EH) instrument covers ~130 eV < E < 28 keV at 16 different energies. Pitch Angle Distributions (PADs) were calculated to look for anisotropies and changes in pitch angle often associated with interaction with whistler waves.

[13] Ion density and solar wind velocity were determined from the PESA Low (PL) detector where density calibrations were made with the WAVES TNR plasma line. Ion distribution functions were calculated for the PESA High (PH) detector in burst mode. Distribution functions were examined for gyrating and/or diffuse ion distributions known to be associated with ULF waves and shocklets, respectively [*Hoppe and Russell*, 1983; *Meziane and D'Uston*, 1998; *Meziane et al.*, 2004].

[14] The relevant shock parameters, determined by J. C. Kasper (Interplanetary shock database, Harvard-Smithsonian Center for Astrophysics, available at http://www.cfa.harvard.edu/shocks/), were the shock normal angle, θ_{Bn}, fast mode Mach number, M_f, and shock strength, N_{i2}/N_{i1}. In this study we define quasi-parallel as $\theta_{Bn} < 45°$ and quasi-perpendicular as $\theta_{Bn} > 45°$. For the five events, θ_{Bn} ranged from 68°–75°, $1.5 < M_f < 4.0$, and $1.5 < N_{i2}/N_{i1} < 4.0$.

[15] Estimates of the electron temperature anisotropies in both the cold dense core (subscript c) and the hotter more tenuous halo (subscript h) can be obtained from full 3D electron distributions. For both EL and EH distributions, average temperatures, parallel (subscript $\|$), and perpendicular (subscript $\perp$) to the magnetic field are computed. Temperature anisotropies, $T_{\perp j}/T_{\| j}$ (j = c or h), were computed for each PAD and compared to threshold conditions for whistler heat flux and anisotropy instabilities of *Gary et al.* [1994, 1999].

[16] The energies used to estimate the halo and core electron temperatures for all the EL distributions were determined by fitting the core to a Maxwellian velocity distribution and the higher-energy halo to a modified Lorentzian [*Thomsen et al.*, 1983a]. The point where the Lorentzian begins to dominate the overall distribution is defined as the break energy, used as the upper bound on the core electrons and the lower bound on the halo electrons. The moments were then calculated directly from the full 3-D electron distributions. The high-energy nonthermal tail in electron distributions, often observed in the solar wind directed away from the sun along the magnetic field, is known as the strahl. This introduces a highly anisotropic peak in the parallel cuts of distribution functions which can increase the difficulty fitting a function to the halo electron distribution. Thus, the strahl electrons were removed in the halo electron fits. The relevant parameters are then calculated from the original electron distributions using the energy bins below the break energy for the core and the energy bins above the break energy for the halo electrons. One should note, the use of energy bin cutoffs instead of the fit functions can lead to increased uncertainty in the estimates of core and halo parameters. The core and halo components overlap in energy, thus one may have core(halo) electrons in their halo(core) moment calculations (see Appendix A for details).

[17] The wave vector and other wave properties were determined using Minimum Variance (MV) analysis [*Khrabrov and Sonnerup*, 1998]. The magnetic field fluctuations were identified and analyzed using a band-pass filter. The frequency ranges for each band-pass filter, determined from spectral analysis, were chosen independently for each shock. MV analysis was then done on specific time ranges to determine the wave vector, **k**, and the polarization. The band-pass filtered waves are shown in both GSE (gray) and MV (color) coordinates with associated hodograms. The [X, Y, Z]-MV coordinates represent the direction parallel to the minimum (red), intermediate (blue), and the maximum (green) variance eigenvectors, respectively, of the spectral matrix. Using the wave vector from MV analysis, the angle of propagation for each wave with respect to the shock normal vector, θ_{kn}, upstream averaged solar wind velocity, θ_{kV}, and the magnetic field, θ_{kB}, were examined.

[18] In the use of MV analysis, we define the eigenvalues of the spectral matrix, from minimum to maximum, as λ_3,

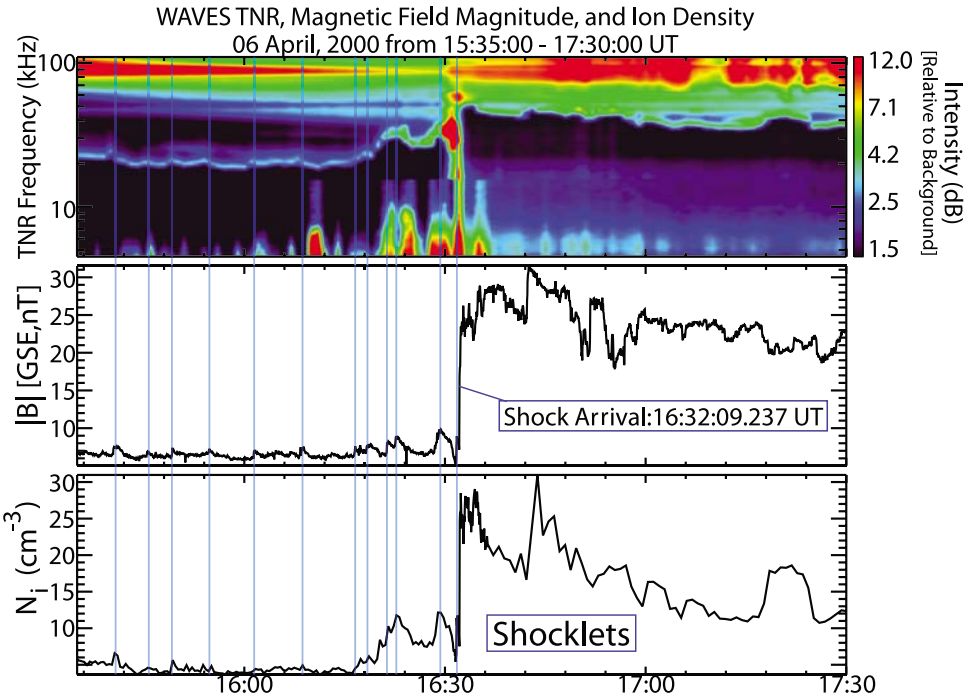

Figure 1. A plot of (top) the electric field intensity as a function of frequency and time, (middle) the magnetic field magnitude (3 s), and (bottom) the ion density from PL on 6 April 2000. The vertical blue lines indicate the location of the 12 shocklets observed upstream of this event. One can see that the magnetic field magnitude and density/thermal line are in phase, consistent with magnetosonic waves.

λ_2, and λ_1. As a general rule for determining whether the MV analysis has yielded a well determined plane circularly polarized wave, we require $\lambda_2/\lambda_3 \geq 10.0$ and $\lambda_1/\lambda_2 \sim 1.0$ if less than 50 field vectors were used in the analysis. For the case where $\lambda_2/\lambda_3 \geq 10.0$ but $1.0 < \lambda_1/\lambda_2 \ll \lambda_2/\lambda_3$, the wave is elliptically polarized. If $\lambda_1/\lambda_2 \gg \lambda_2/\lambda_3 \sim 1.0$ then the wave is linearly polarized and the **k** vector cannot be trusted. These assumptions hold for data with small isotropic Gaussian noise [*Khrabrov and Sonnerup*, 1998]. Single satellite measurements introduce another complication. Though the plane orthogonal to the **k** vector may be well determined, the sign of the vector cannot be known without at least one component of the electric field or another satellite measurement [*Hoppe et al.*, 1981, 1982; *Hoppe and Russell*, 1983].

3. Shock Observations

3.1. Unusual Event of 6 April 2000

[19] Five quasi-perpendicular IP shocks were analyzed in this study. Four of the events had waves with characteristics similar to previous bow shock studies [*Farris et al.*, 1993; *Sentman et al.*, 1983] and IP shock observations [*Russell et al.*, 1983]. The 6 April 2000 event, however, showed characteristics not previously seen at an IP shock. Figure 1 shows the unusual IP shock of 6 April 2000 with the 12 observed shocklets labeled with blue lines in Figure 1. The image illustrates the relationship between magnetic field magnitude and ion density. The 6 April 2000 event is the strongest shock examined in this study with $M_f \sim 4$, $\theta_{Bn} \sim 68°$, and $N_{i2}/N_{i1} \sim 4$. Figure 1 (top) shows the electric field intensity with respect to background from the WAVES TNR. Upstream of the shock one can easily see the plasma line which is proportional to the root of the plasma density. Thus, when the plasma line increases in frequency, the density has increased also. Note that the TNR data shown is one minute averages and on a log scale, thus the relative changes in phase with the magnetic field (Figure 1, middle) is not always obvious. To aid the eye, Figure 1 (bottom) plots the ion density from PL. One can clearly see that the magnetic field magnitude and ion density are in phase, consistent with magnetosonic waves.

[20] Figure 2 shows the same event as Figure 1, on a shorter time scale, with the magnetic field magnitude scaled to emphasize the shocklets seen upstream (indicated by the blue arrows). The IP shock was observed by Wind at 1632:09.237 UT (i.e., the far right-hand side of Figure 2 (top) or roughly 3 s after shocklet B). Figure 2 (bottom) shows examples of two shocklets with waves on the leading edge consistent with a RH whistler mode. The structure of the shocklet is labeled in shocklet B. Shocklets 1, 3–5, 7, and 9–12 all had clearly formed waves on their leading edges. These waves had RH polarizations with respect to the magnetic field and an increase in ion density coincident with the increase in $|\mathbf{B}|$, consistent with magnetosonic whistlers and magnetosonic waves.

[21] Figures 3 and 4 show examples of the analysis done on each wave. For each wave event in Figures 3 and 4, there are three sets of plots. The left-hand set of plots in wave events A–D are the GSE (gray scale) components, the middle set plots the MV (color scale) components, and the right-hand set of plots shows the hodograms, B_y versus B_x, B_z versus B_x, and B_z versus B_y. The time ranges for the selected subintervals seen in wave events A–C, were chosen

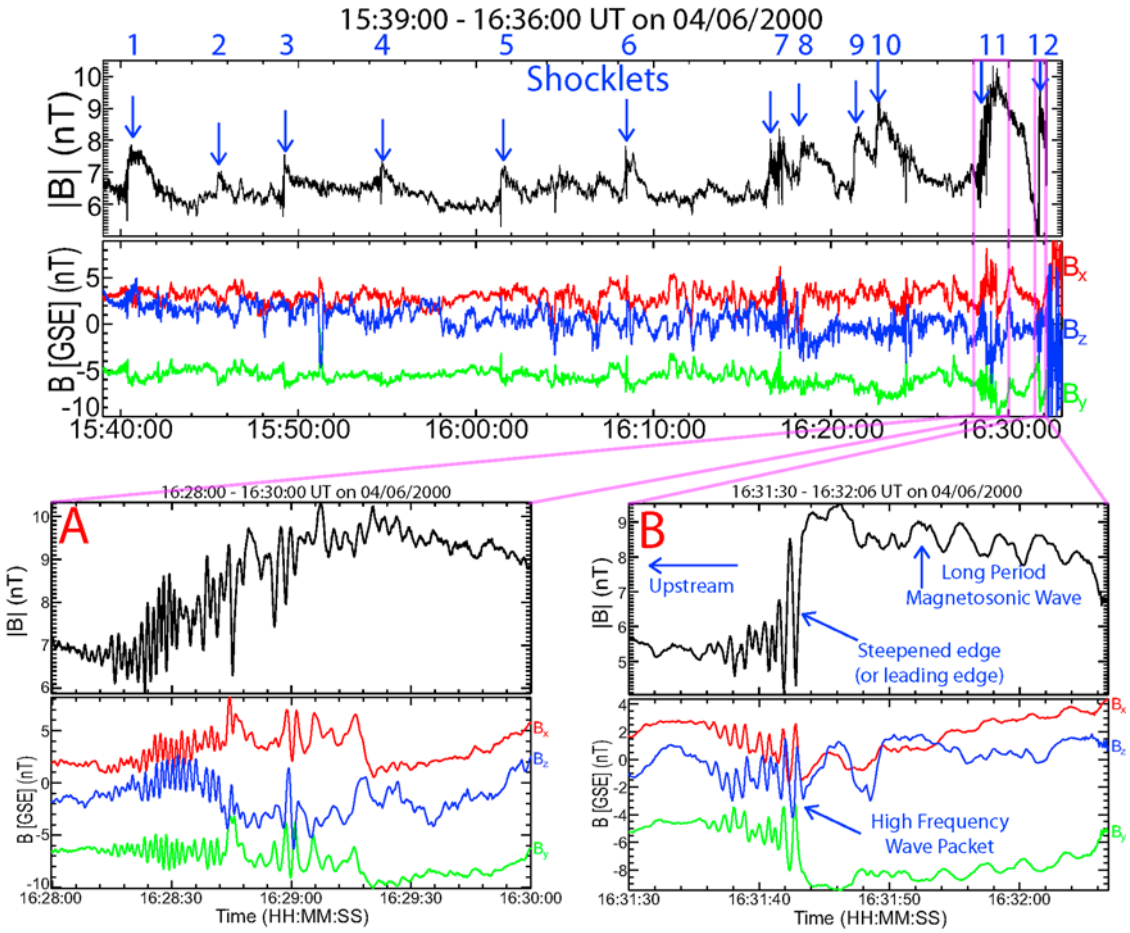

Figure 2. A plot of the magnetic fields for the unusual IP shock of 6 April 2000. The shock arrival time was 1632:09.237 UT. (top) The magnetic field strength, $|\mathbf{B}|$ (nT), followed by the field components in GSE coordinates from 1539:00–1636:00 UT. In Figure 2 (top), the location of each shocklet observed for this event is labeled with a blue number and an arrow. (bottom) The two shocklets which will be analyzed in detail in this paper are labeled A and B (Figures 3 and 4 show a more detailed picture of each shocklet). Figure 2 (top) has been scaled down to show the shocklets more clearly because the IP shock itself jumps to over 30 nT downstream (only a few seconds after shocklet B).

to maximize the intermediate to minimum eigenvalue ratio, seen in red in each wave event. In every wave analysis presented and every wave examined (125 different analyses for all five IP shocks), $\lambda_2/\lambda_3 \geq 10.0$ and 56 cases had $\lambda_2/\lambda_3 \geq 50.0$.

[22] The use of multiple band pass filters on the shocklets revealed that their wave vectors remained relatively unchanged between the different frequency bands chosen for our filters. This is illustrated clearly in wave events A, C, and D of Figure 4. The time intervals for each case are similar, but each case was filtered over a different frequency bin. The wave vector is the same for each case within uncertainties. We also observed a clear dependence of the peak frequency on the distance from the steepened edge of the shocklets, where the higher-frequency waves were seen first, followed by the lower-frequency waves as the shocklets convected over the satellite. This is consistent with the frequency dependence of magnetosonic whistlers, whose group velocities increase with increasing frequency. This result is also seen in simulations [*Omidi and Winske*, 1990; *Scholer*, 1993; *Scholer et al.*, 2003; *Tsubouchi and Lembège*, 2004].

[23] The difference in polarization between wave events A, C, and D in Figure 4 can be explained by projection effects due to single satellite measurements using only magnetic field measurements. In the spacecraft frame, wave events A, B, and D in Figure 3 are LH polarized with respect to the propagation direction, but all wave events in Figures 3 and 4 show a RH sense with respect to the magnetic field, characteristic of whistler modes. Wave event C in Figure 3 and wave events A and B in Figure 4 are RH polarized both with respect to the wave vector and the magnetic field.

3.2. Comparison of the 6 April 2000 Event to the Four Typical Events

[24] As mentioned above, four of the IP shocks had waves with characteristics consistent with previous shock studies. Figure 5 shows the magnetic field magnitude and GSE components for the four IP shocks with typical characteristics. The four events with precursor waves are much lower Mach number shocks ($M_f \leq 2.3$) than the

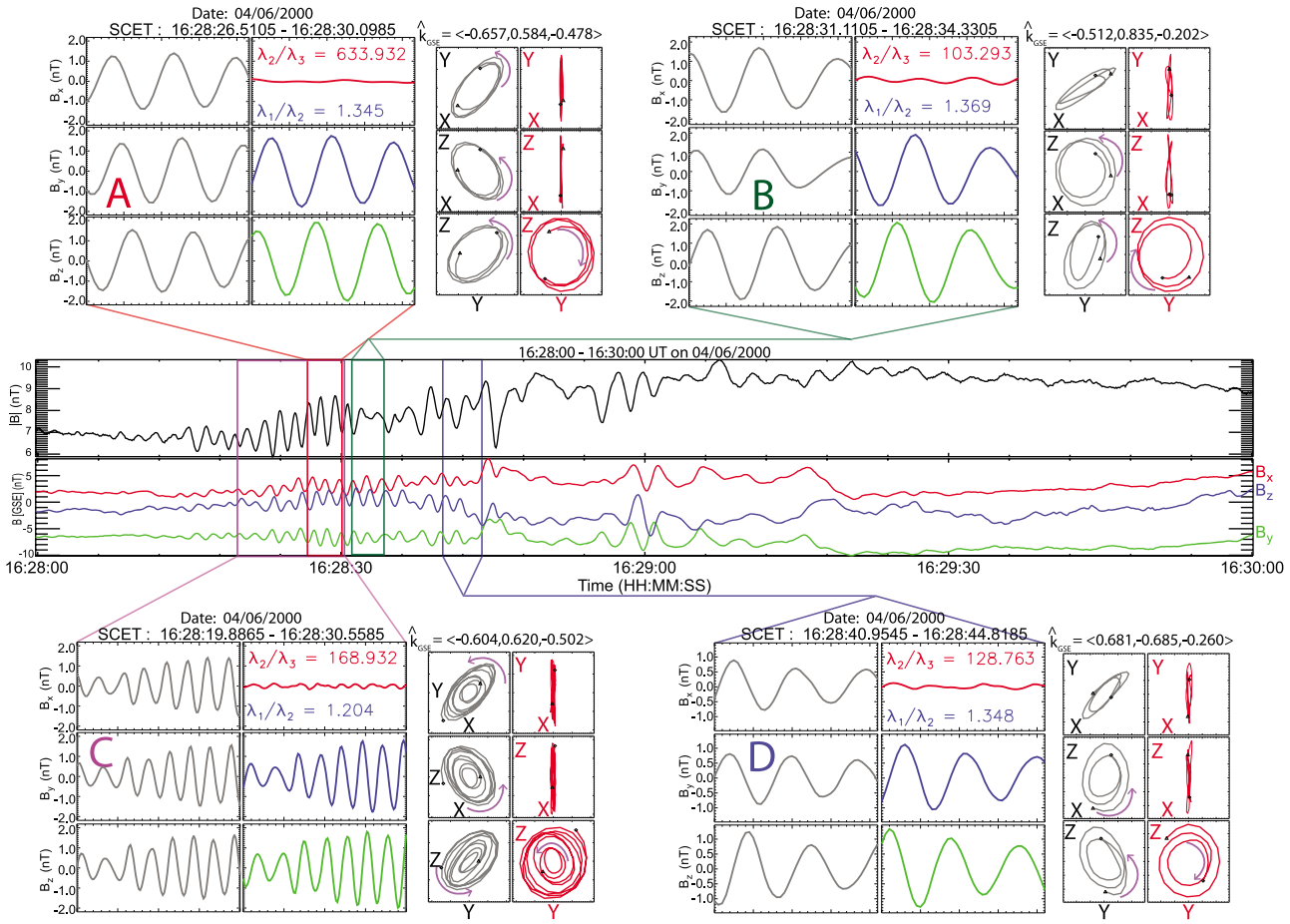

Figure 3. An example of MV analysis on the leading whistler waves of shocklet A in Figure 2. The frequency ranges and angles of propagation are 0.5 Hz < f < 1.0 Hz and θ_{kB} = 35°(145°) for wave event A, 0.5 Hz < f < 1.0 Hz and θ_{kB} = 14°(166°) for wave event B, 0.6 Hz < f < 3.0 Hz and θ_{kB} = 41°(139°) for wave event C, and 0.6 Hz < f < 3.0 Hz and θ_{kB} = 18°(162°) for wave event D. The eigenvalue ratios from the MV analysis are also shown with the MV estimate of the **k** vector direction in GSE coordinates above each hodogram. The purple arrows indicate the direction of rotation for each respective plot.

unusual event ($M_f \sim 4$), consistent with theory [*Mellott and Greenstadt*, 1984].

[25] Figure 5 (top) shows examples of lower Mach number quasi-perpendicular shocks with a leading wave train and a relatively stable transition from up to downstream. Figure 5 (bottom) shows examples of higher Mach number shocks with a much more turbulent transition. The relevant shock parameters are given in the green box. The waves in Figure 5 are similar to the precursor whistler waves observed by *Russell et al.* [1983] in frequency and their propagation angle with respect to the shock normal, θ_{kn}. Since θ_{kn} is not small it is not likely that these waves are phase standing with respect to the shock. The precursors did have high degrees of RH polarization (nearly circular) with respect to the magnetic field, and propagate obliquely to the field with > 95% having propagation angles θ_{kB} > 20°. However, *Russell et al.* [1983] found that 75% of the precursors had propagation angles θ_{kB} < 20°.

[26] The whistler precursor waves and shocklets shared some characteristics. The range of θ_{kB} values can be seen in Figure 6. There is an obvious difference between the whistlers upstream of the four typical events (Figure 6, bottom) and the 12 shocklets (Figure 6, top) observed upstream of the unusual IP shock on 6 April 2000. The shocklets have a much broader range of θ_{kB} and tend to be more oblique than the precursor whistler waves. If the shocklets are in fact magnetosonic whistlers, the higher values of θ_{kB} would be consistent with their more compressive nature than that of the precursor whistlers. Almost 80% of the shocklets observed for the 6 April 2000 event with SC frame frequencies f > 0.45 Hz had $\theta_{kB} \leq 45°$, consistent with bow shock observations [*Hoppe et al.*, 1981, 1982; *Hoppe and Russell*, 1983; *Russell et al.*, 1971] and cometary foreshock observations [*Le et al.*, 1989]. Over 90% of the whistler observed for the 4 IP shocks without shocklets had $\theta_{kB} \leq 45°$, consistent with theory [*Gary et al.*, 1994, 1999] and observations of whistler precursor waves at IP shocks [*Russell et al.*, 1983]. There were no distinguishing characteristics in θ_{kn} or θ_{kV} between the shocklets and precursor whistlers.

3.3. Particle Data

[27] The wave events of Figures 3 and 4 show a clear relationship with the low- to middle-energy electron distributions. Previous studies of whistler waves at shocks suggested a relationship between whistler mode generation

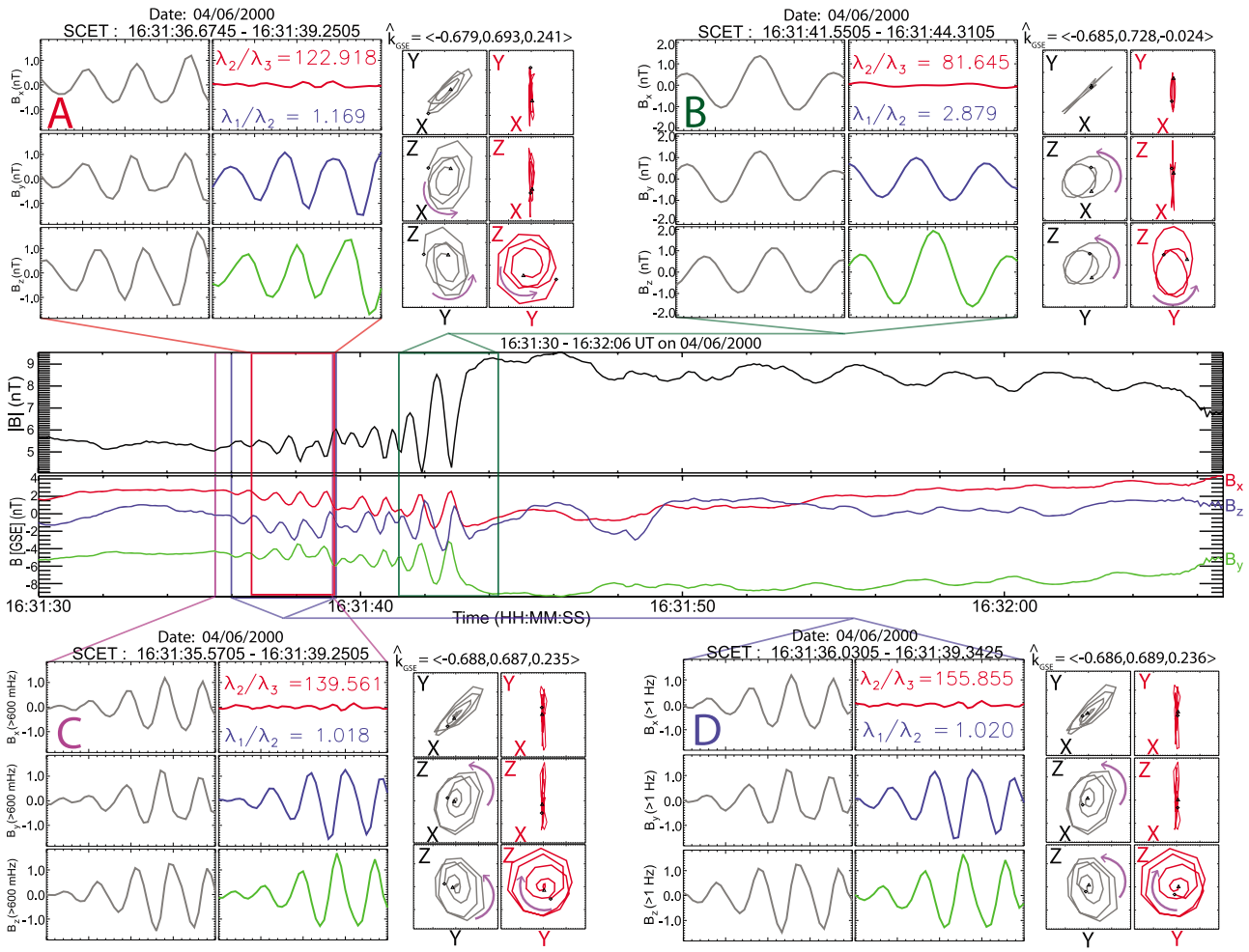

Figure 4. Another example of MV analysis on the leading whistler waves of a shocklet seen just upstream from the IP shock on 6 April 2000 (see shocklet B in Figure 2). The format matches that of Figure 3 but with different frequency ranges. The frequency ranges and angles of propagation are 0.6 Hz < f < 3.0 Hz and $\theta_{kB} = 27°(153°)$ for wave event A, 0.45 Hz < f < 1.0 Hz and $\theta_{kB} = 49°(131°)$ for wave event B, f > 0.6 Hz and $\theta_{kB} = 25°(155°)$ for wave event C, and f > 1.0 Hz and $\theta_{kB} = 26°(154°)$ for wave event D.

and electrons [*Tokar et al.*, 1984; *Tsurutani et al.*, 1983]. *Gary et al.* [1994] determined the threshold conditions for whistler heat flux and whistler anisotropy instabilities for typical solar wind conditions. They found that the instabilities were strongly dependent on the core parallel plasma beta, $\beta_{\|c}$, the ratio of parallel halo temperature to parallel core temperature, $T_{\|h}/T_{\|c}$, and the temperature anisotropy of the halo, $T_{\perp h}/T_{\|h}$. Using linear Vlasov theory, *Gary et al.* [1999] showed that the halo temperature anisotropy has a larger effect on the heat flux instability than the core temperature anisotropy. They also found that the heat flux-driven whistler mode was always unstable for $T_{\perp h}/T_{\|h} > 1.01$ and always stable for $\beta_{\|c} \leq 0.25$. In the cases where $T_{\perp h}/T_{\|h} > 1.01$ but $T_{\|h}/T_{\|c}$ is small, *Gary et al.* [1994] suggested that a whistler anisotropy instability may be excited even in the absence of a relative drift between the core and halo electrons. Thus if the halo electrons initially meet this criteria, the whistler anisotropy instability would dominate over the whistler heat flux instability. The whistler anisotropy instability acts to reduce the relative drift between the halo and core electrons (if present) and an isotropize the halo temperatures. $T_{\perp h}/T_{\|h}$ would reduce faster than the halo/core drift (and $T_{\|h}/T_{\|c}$) could reduce causing the electron distributions to become unstable to a whistler heat flux instability. In the case of large $T_{\|h}/T_{\|c}$ and small $T_{\perp h}/T_{\|h}$, the whistler heat flux instability would initially dominate over the whistler anisotropy instability. This instability would increase $T_{\perp h}/T_{\|h}$ slower than it could reduce $T_{\|h}/T_{\|c}$ [*Gary et al.*, 1994].

[28] The electron pitch angle distributions (PADs) for three wave events are plotted in Figures 7–9. The primary influence of whistler heat flux instability is to pitch angle scatter the halo electrons through a cyclotron resonance. There is a clear increase in the halo electron temperature anisotropy, $T_{\perp h}/T_{\|h}$ (see Table 1), as one crosses each wave, consistent with normal cyclotron resonance increasing the transverse energy of the electrons. $T_{\perp c}/T_{\|c}$ follows the same pattern, but the increase is not as dramatic. The threshold conditions for a whistler heat flux or anisotropy instability [*Gary et al.*, 1994, Figures 7 and 8] are met by most of the EL PADs up and downstream of the waves in Figures 7–9. There are, however, differences in our estimates of n_{he}/n_e,

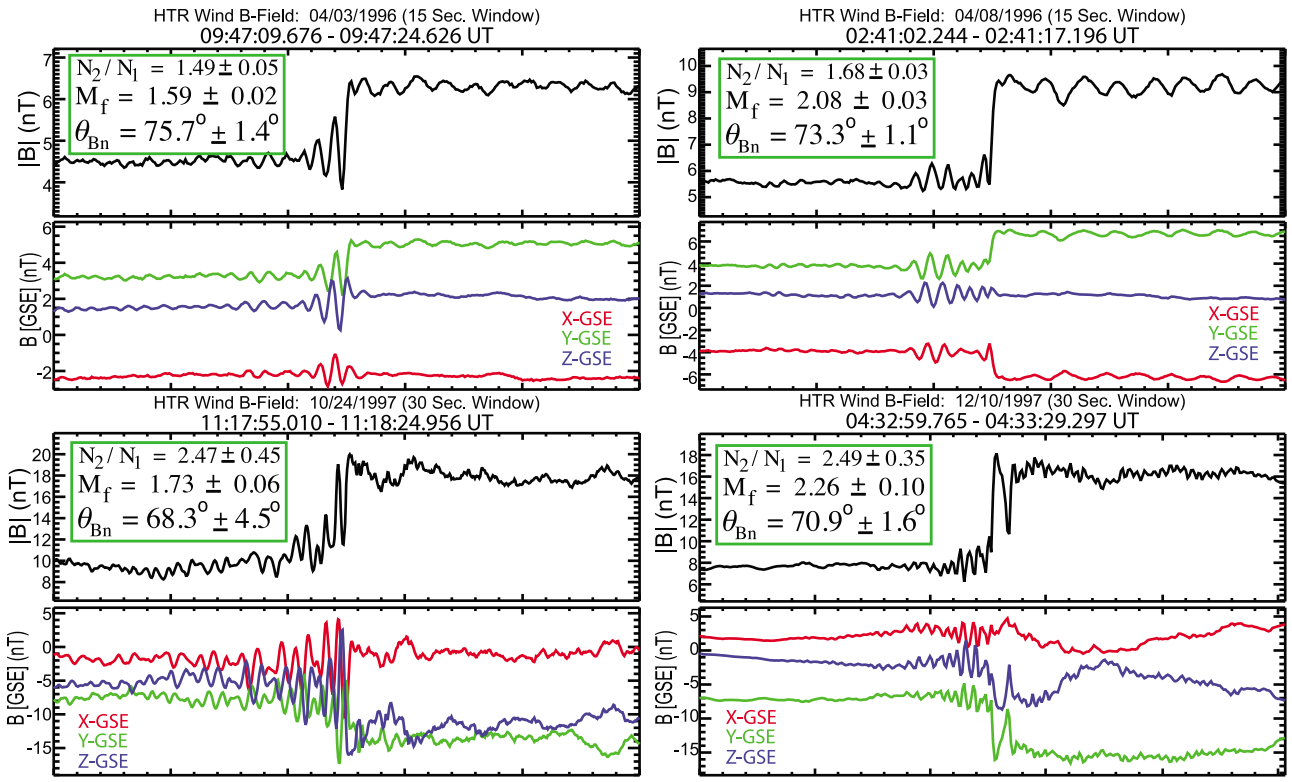

Figure 5. The four IP shocks without upstream shocklets show examples of typical low-frequency magnetic fluctuations seen upstream from quasi-perpendicular shocks. (top) Examples of laminar quasi-perpendicular shocks with leading precursor whistler waves (3 April 1996 and 8 April 1996). (bottom) A far more turbulent transition from upstream to downstream (24 October 1997 and 10 December 1997). All exhibit leading precursor whistler waves.

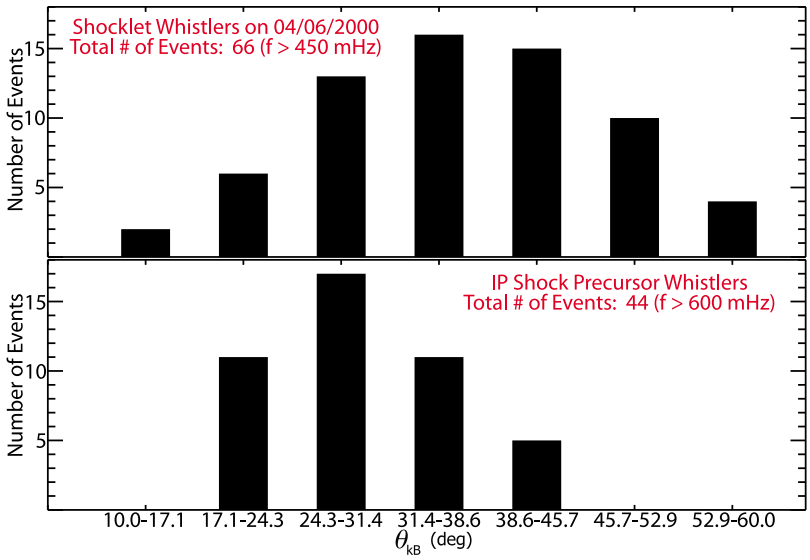

Figure 6. Histograms comparing the angle of propagation with respect to the magnetic field for the IP shock precursor whistler waves and the shocklet whistlers. (top) The range of angles for all band-pass frequency bins greater than 0.45 Hz but only for the 12 shocklets (each shocklet has multiple waves as seen in Figures 3 and 4) observed on 6 April 2000. (bottom) The range of angles for all band-pass frequency bins greater than 0.6 Hz for the four IP shocks without shocklets. The horizontal and vertical axes are on the same scales for both plots. Multiple frequency ranges were chosen for each IP shock.

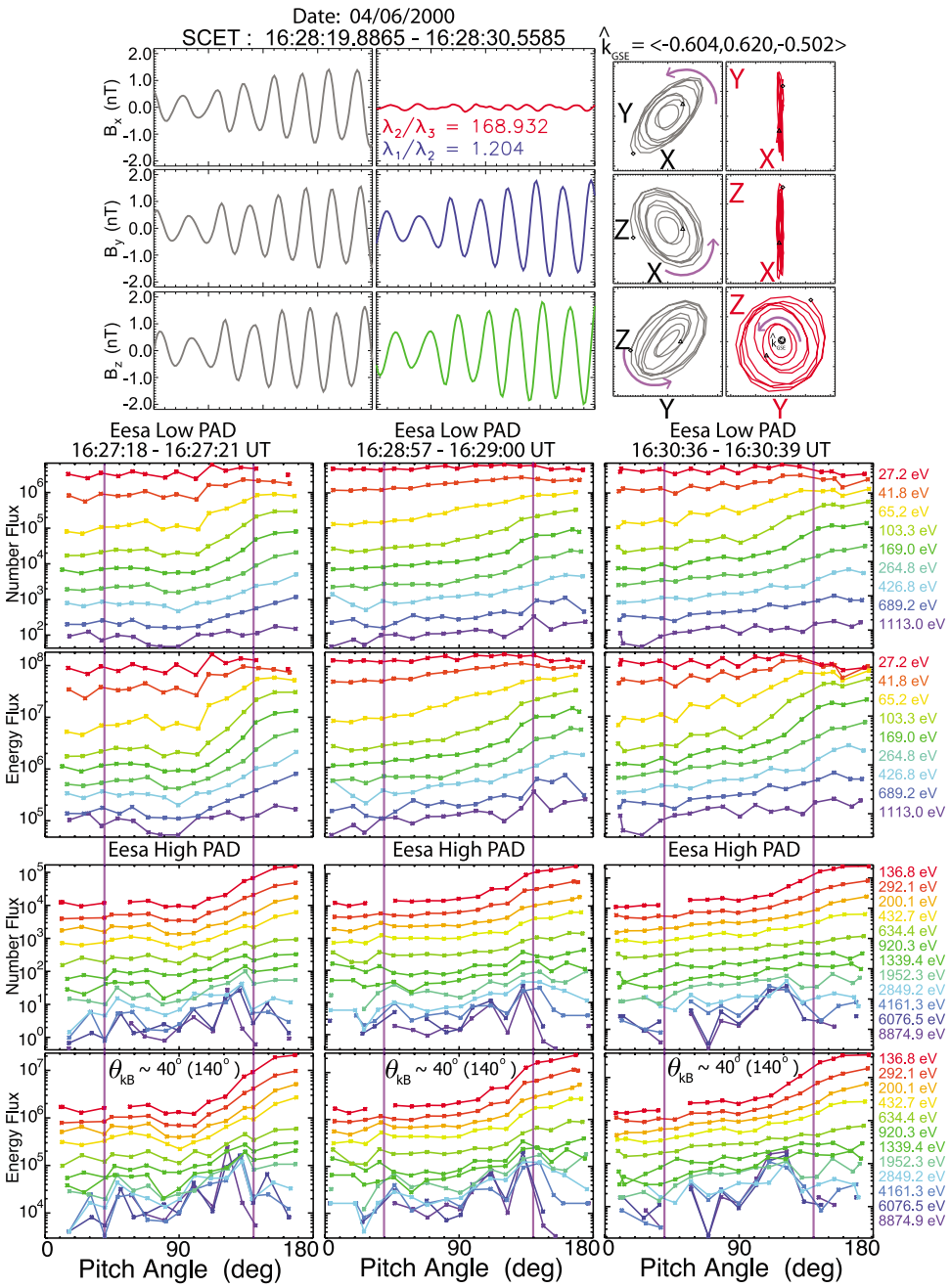

Figure 7. Comparison of wave polarization and electron distributions (wave event D from Figure 3) with six pitch angle distributions (PADs) from the Eesa Low (EL) and High (EH) instruments. Each PAD is plotted in number (# $s^{-1}sr^{-1}cm^{-2}eV^{-1}$) and energy (eV $s^{-1}sr^{-1}cm^{-2}eV^{-1}$) flux. The energies plotted range from 27 to 1113 eV for EL and 137 to 8875 eV for EH. The frequency range is 0.6 Hz < f < 3 Hz for the band-pass filter used on the MFI data and θ_{kB} = 40°(140°). The vertical lines on the PADs represent an average estimate of the propagation angle, θ_{kB}, for the wave shown. The electron temperature anisotropies and other parameters can be found in Table 1.

distributions used to model the halo electrons, and definition of heat flux from those of *Gary et al.* [1994]. Our estimates of n_{he}/n_e were often a factor of 10 or more smaller than the estimates used by *Gary et al.* [1994] (~0.05) for the PADs shown herein (see Table 1). *Gary et al.* [1994] used bi-Maxwellian distributions to model both core and halo electrons whereas we fit the halo distributions to modified Lorentzian distributions. *Gary et al.* [1994] used a simplified version of the heat flux from *Feldman et al.* [1975] whereas we calculated the full heat flux tensor, assuming it symmetric, and derived a vector from that tensor.

[29] One can see that $T_{\perp h}/T_{\parallel h}$ increases across the waves in Figures 8 and 9 (from 0.55 for PAD 1631:32–1631:35 UT to 1.02 for PAD 1631:44–1631:47 UT shown in Table 1, an increase of ~85%). *Gary et al.* [1994] found that the whistler

Table 1. Wind 3DP Electron Stats on 6 April 2000

Start-End Time (UT)	T_{ce} (eV)	T_{he} (eV)	$T_{\perp c}/T_{\|c}$	$T_{\perp h}/T_{\|h}$	n_{ce} (cm^{-3})	n_{he} (cm^{-3})	$T_{\|h}/T_{\|c}$	$\beta_{\|c}$
				Eesa Low				
1627:18–1627:21	10.80	125.34	0.86	0.66	5.95	0.030	13.69	0.86
1628:57–1629:00	10.56	125.52	0.99	0.84	9.95	0.039	13.19	0.71
1630:36–1630:39	11.14	117.85	0.95	0.91	9.03	0.051	10.86	0.70
				Eesa Low Burst				
1631:32–1631:35	10.02	117.29	0.70	0.55	5.02	0.026	13.42	1.16
1631:35–1631:38	10.40	120.33	0.73	0.59	4.74	0.026	13.07	1.02
1631:38–1631:41	10.28	127.57	0.73	0.55	5.16	0.023	14.53	1.14
1631:41–1631:44	11.54	129.47	0.94	0.84	6.08	0.039	12.03	0.79
1631:44–1631:47	11.16	126.61	1.02	1.02	10.42	0.050	11.37	0.75

heat flux instability reduced $T_{\|h}/T_{\|c}$ but increase $T_{\perp h}/T_{\|h}$ at a faster relative rate. We observed $T_{\|h}/T_{\|c}$ to decrease across the waves (from 13.4 for PAD 1631:32–1631:35 UT to 11.4 for PAD 1631:44–1631:47 UT, a decrease of ~15%). The same observation can be made for the wave in Figure 7. $T_{\perp h}/T_{\|h}$ increases across the wave (0.65 for PAD 1627:18–1627:21 to 0.91 for PAD 1630:36–1630:39, an increase of ~40%) and $T_{\|h}/T_{\|c}$ decreases (13.7 for PAD 1627:18–1627:21 to 10.9 for PAD 1630:36–1630:39, a decrease of ~20%). Notice in both cases $T_{\perp h}/T_{\|h}$ increases at a faster relative rate than $T_{\|h}/T_{\|c}$ decreases, consistent with the simulation results by *Gary et al.* [1994].

[30] If we assume that the rest frame frequencies of the observed waves are consistent with *Hoppe et al.* [1982] and use our measured θ_{kB}, then the resonant energies for normal cyclotron resonance are 250 eV $\leq E_{res} \leq$ 4 keV for the event in Figure 7, and 200 eV $\leq E_{res} \leq$ 3 keV for the wave in Figure 8. In Figure 7, most of the energy bins (65–689 eV for EL and 136 eV to 3 keV for EH) of the PADs which undergo the greatest change across the wave are within the estimated resonant energy range. The PADs in Figures 8 and 9 are also consistent with the resonant energies showing the greatest changes from the PAD at 1631:32 UT in Figure 8 to the PAD at 1631:44 UT in Figure 9. The average increase in pitch angle of the electrons in this energy range across the waves would be consistent with pitch angle diffusion were we observing the same distribution in time. It is difficult to say whether the strong anisotropies in the electron PADs downstream of the shocklets are a consequence of their traversal of the shocklets or if

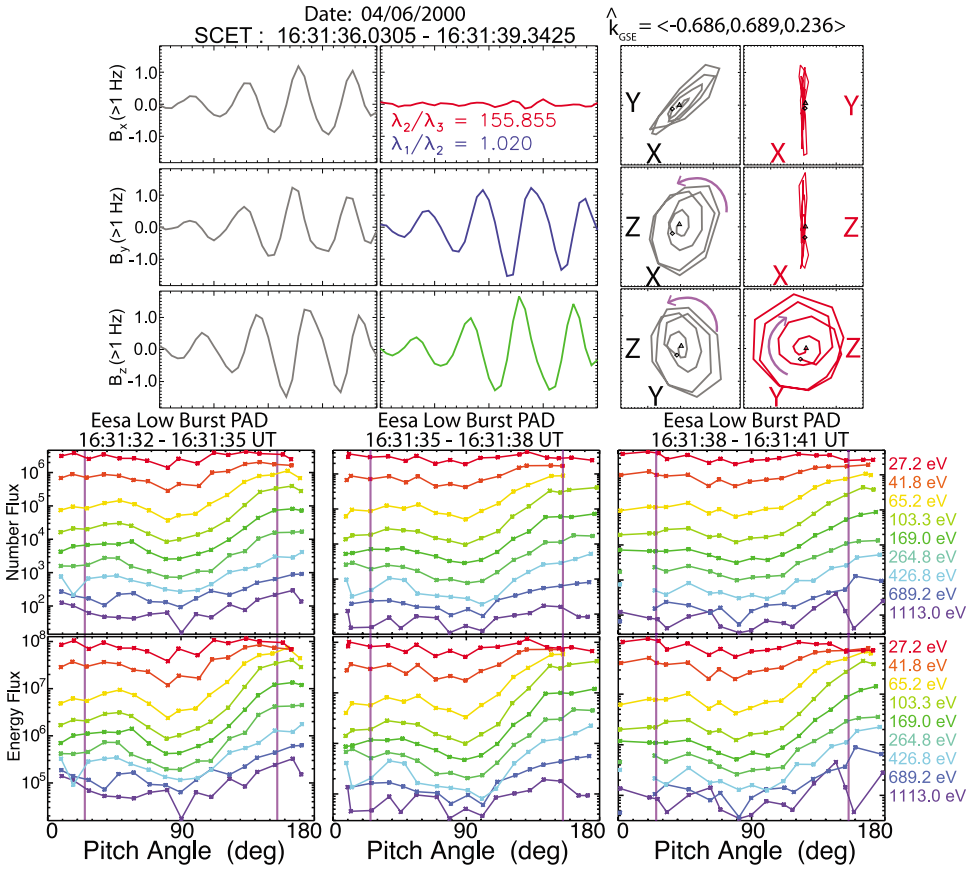

Figure 8. The same format as Figure 7. The frequency range is f > 1.0 Hz and θ_{kB} = 25°(155°). The electron temperature anisotropies and other parameters can be found in Table 1.

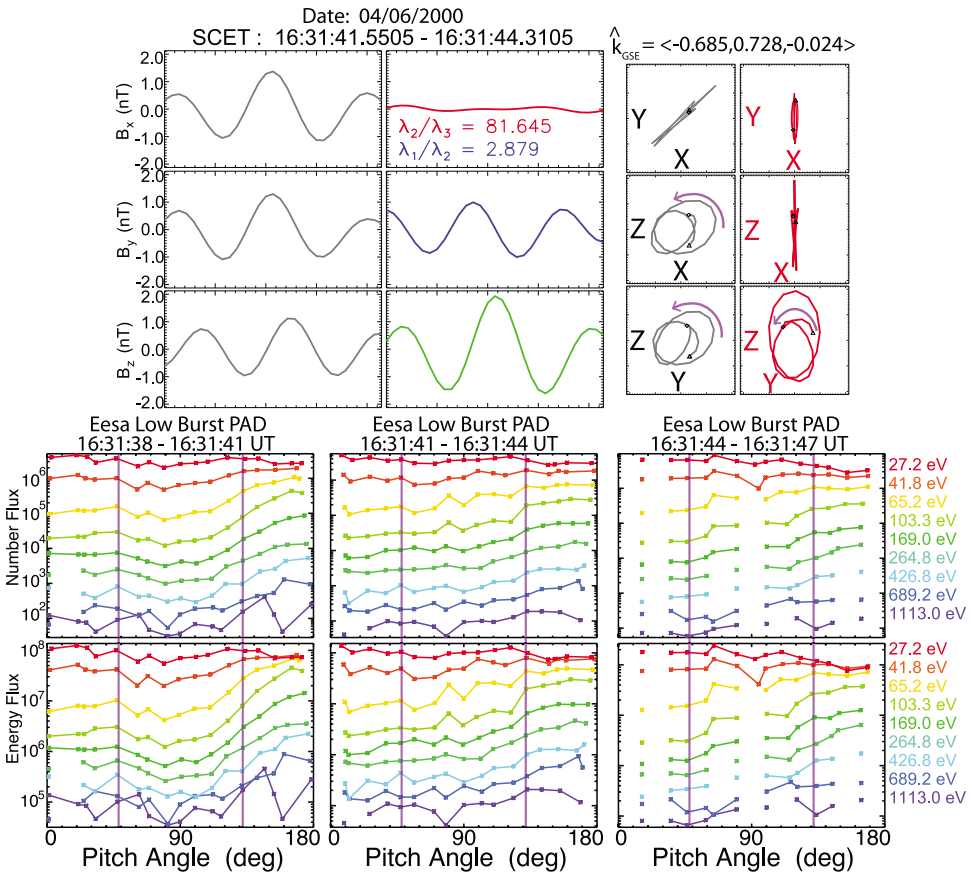

Figure 9. The same format as Figure 8 except that the wave occurs roughly 2.5 s later (see Figure 7 for more details). The frequency range is 0.45 Hz < f < 1.0 Hz and $\theta_{kB} = 49°(131°)$. The electron temperature anisotropies and other parameters can be found in Table 1.

their downstream location with respect to the shocklet results in the isotropization through leakage. Leakage is the process where the downstream electrons with large pitch angles are restricted to the downstream by the shocklet's magnetic fields, while the lower pitch angle electrons can move freely upstream [*Larson et al.*, 1996; *Thomsen et al.*, 1983b].

[31] The electron heat flux, or more appropriately, the kinetic energy flux in the plasma rest frame, was calculated to more thoroughly examine the instability thresholds discussed by *Gary et al.* [1994, 1999]. Each 3DP electron distribution was first transformed into the solar wind frame, without ignoring the spacecraft potential, and then the first four moments of the distribution function were calculated. The heat flux, in its general form, is the third moment of the distribution function. Assuming some symmetries, the third rank tensor can reduce to a simple second rank tensor, where the sum of the i^{th} row results in the i^{th} component of the resultant heat flux vector. The mathematical form can be expressed as:

$$\vec{\mathbf{q}} = \frac{m_e}{2} \int d^3v \vec{\mathbf{v}} v^2 f(\vec{\mathbf{x}}, \vec{\mathbf{v}}, t) \qquad (1)$$

where m_e is the electron mass, $\vec{\mathbf{v}}$ the velocities, and $f(\vec{\mathbf{v}}, \vec{\mathbf{x}}, t)$ represents a general form of the distribution function. The vector is then rotated into an appropriate coordinates system.

[32] The angle between the wave vectors and heat flux vectors calculated for each PAD change from ~20° to ~27° for 1631:32–1631:44 UT. Also, the magnitude of the heat flux changes from ~49 to ~85 keV cm^{-3} km/s for 1631:32–1631:44 UT. Thus, the heat flux magnitude, angle between wave vector and heat flux, and angle between heat flux vector and magnetic field all peak in the 1631:44–1631:47 UT PAD which is just downstream of the peak amplitude of shocklet B in Figure 2.

[33] The electron distributions at the unusual event show strong heating in the downstream region. The downstream region of the 6 April 2000 event had broad flattop distributions downstream, thought to result from strong current-driven ion acoustic waves [*Thomsen et al.*, 1983a]. The 10 December 1997 event showed weak flattop distributions downstream for a few seconds, followed by a Maxwellian hotter than the upstream distributions. The flattop distributions lasted for over an hour downstream of the 6 April 2000 IP shock.

[34] The halo electrons have strong anisotropies in the downstream of the 6 April 2000 event. The halo electrons show strong heating perpendicular to the magnetic field with a remarkably low change in the parallel halo temperature. In fact, the 6 April 2000 event is the only IP shock to show a global decrease in $T_{\|h}$ and global increase in $T_{\perp h}/T_{\|h}$ across the shock. The preferential perpendicular heating of the halo electrons may be explained by the

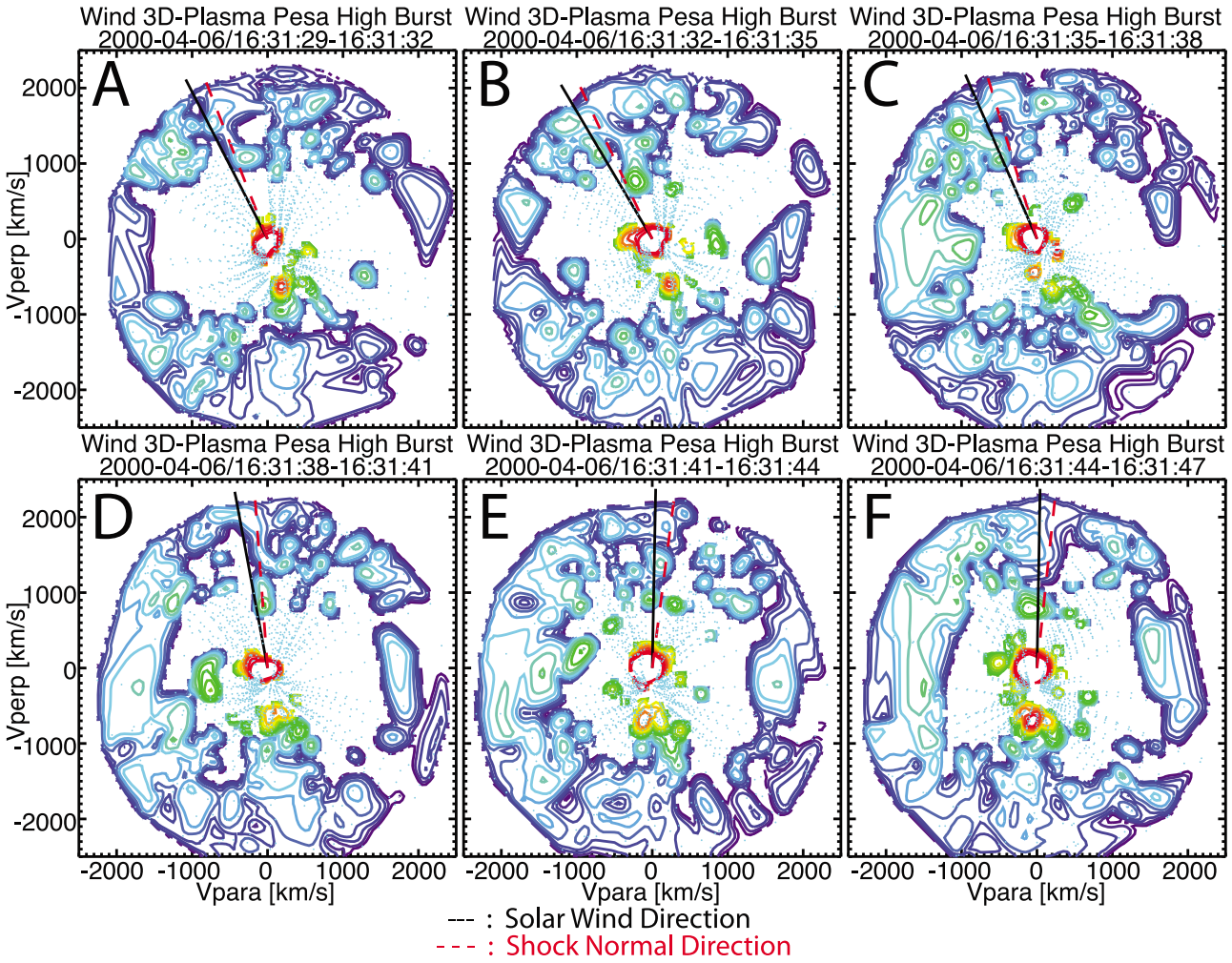

Figure 10. A series of contour plots of the ion distribution function from PHB from 1631:29 UT to 1631:47 UT. The high-energy diffuse ions are seen as the semi-isotropic ring between 1000 and 2000 km/s. These distributions are observed simultaneously with shocklet B in Figure 2.

efficiency of the pitch angle scattering discussed by *Saito and Gary* [2007] which showed a preferential efficiency with higher kinetic energy electrons. The reason for the low heating in the parallel halo electrons is not known at this time.

[35] The fact that shocklets were observed upstream at only one of the five IP shocks raises the question what characteristics of the 6 April 2000 event might lead to their generation. It is highly likely that the 6 April 2000 event is a supercritical shock (i.e., requires particle reflection for energy dissipation), which may explain why shocklets are observed upstream of this event and none of the others. Particle reflection could explain the difference in heating between the 6 April 2000 event and the other four. Recent observations (L. B. Wilson III et al., Large amplitude electrostatic waves observed at a supercritical interplanetary shock, manuscript in preparation, 2009) have shown evidence of the modified two stream instabilities discussed by *Matsukiyo and Scholer* [2006] which were shown to strongly heat the electrons and ions. The core electrons show significant heating ($T_{c2}/T_{c1} \gtrsim 3.5$) which one would expect from an interaction with electrostatic waves [*Thomsen et al.*, 1985; Wilson et al., preprint, 2009] and/or electromagnetic modes like the modified two stream instability [*Matsukiyo and Scholer*, 2006]. Thus, ion reflection is likely playing a more significant role in energy dissipation than at the other lower Mach number events [*Thomsen et al.*, 1985].

[36] Most studies of shocklets at the terrestrial bow shock focused on ion distributions. Shocklets were observed to have a location dependence in the terrestrial ion foreshock. They are observed in association with diffuse ion distributions, a characteristic distribution seen in deeper regions (i.e., further from the sun) of the foreshock [*Hoppe et al.*, 1981, 1982; *Hoppe and Russell*, 1983]. Figure 10 shows examples of diffuse ions seen simultaneously with shocklet B in Figure 2. The plots are PHB distribution functions plotted with the horizontal axis parallel to the ambient magnetic field in the plane created by the magnetic field and solar wind velocity. In each plot, the solar wind direction (black line) and shock normal direction (red line) are projected onto the distributions for reference.

4. Conclusions

[37] We present observations on two classes of waves with frequencies from 0.25 Hz < f < 10 Hz at five quasi-

perpendicular IP shocks. The first class of waves is a nonphase standing precursor whistler observed just upstream of four of the IP shocks examined in this study. The second class is a steepened magnetosonic wave, with a leading magnetosonic whistler wave train, called a shocklet. The shocklets and precursor whistlers are observed in association with electron distributions unstable to whistler heat flux and/or whistler anisotropy instabilities. The precursor whistlers at the four IP shocks without shocklets were highly oblique with propagation angles with respect to the magnetic field of $20^\circ \leq \theta_{kB} \leq 45^\circ$ and propagation angles with respect to the shock normal of $29^\circ \leq \theta_{kn} \leq 75^\circ$. Almost all of the shocklet whistlers observed upstream of the 6 April 2000 event had propagation angles with respect to the magnetic field of $\theta_{kB} \leq 45^\circ$. This is the first study to observe shocklets upstream of a quasi-perpendicular IP shock and whistler waves simultaneously with electron distributions unstable to whistler heat flux and/or whistler anisotropy instabilities.

[38] The strongest event, on 6 April 2000, is the most unusual shock in our study because it is the only event with shocklets. We observed 12 shocklets upstream ($\leq$ 1 h of shock ramp) of the shock. Almost 80% of the shocklets had $\theta_{kB} \leq 45^\circ$, consistent with the cometary bow shock study by *Le et al.* [1989] and terrestrial bow shock studies [*Hoppe et al.*, 1981, 1982; *Hoppe and Russell*, 1983; *Russell et al.*, 1971]. It is likely that shocklets only occurred at the 6 April 2000 event because of its unusually high Mach number ($M_f \sim 4$). The high Mach number and quasi-perpendicular nature of the shock suggest that it is a supercritical shock, thus requiring ion reflection to dissipate energy. Ion reflection has been shown to be an important aspect of ULF wave generation in observations [*Hoppe and Russell*, 1983; *Thomsen et al.*, 1983b; *Meziane and D'Uston*, 1998] and simulations [*Omidi and Winske*, 1990; *Scholer et al.*, 2003; *Tsubouchi and Lembège*, 2004]. Shocklets are often seen in association with diffuse ion distributions [*Hoppe et al.*, 1981; *Hoppe and Russell*, 1983] and the ULF waves observed by *Hoppe and Russell* [1983] were seen to steepen into shocklets with associated leading magnetosonic whistler wave packets when in regions of diffuse ions. Simulation studies have supported these observations and suggest that diffuse ions may be a necessary factor for ULF waves steepening into shocklets [*Omidi and Winske*, 1990; *Scholer et al.*, 2003; *Tsubouchi and Lembège*, 2004]. Thus, the simultaneous observation of the diffuse ion distributions in Figure 10 and the wave in shocklet B in Figure 2 supports our hypothesis that these magnetic structures are in fact shocklets.

[39] The major differences in electron moments between the 6 April 2000 event and the other four occurred primarily in the halo electrons. The only IP shock to show a strong global increase ($\sim$ a factor of 2) in $T_{\perp h}/T_{\| h}$ from upstream to downstream was the 6 April 2000 event. The relative heating between the electron halo and core ($T_{\| h}/T_{\| c}$) components is more dramatically affected in the 6 April 2000 event than any other studied decreasing by a factor of $\gtrsim$ 3.5 across the IP shock (other events increase by $\leq$ 2). The decrease is due to the large increase in $T_{\| c}$ and slight decrease in $T_{\| h}$ across the shock. The $\beta_{\| c}$ is almost always $\leq$ 1.0 upstream (within an hour of the ramp) of the 6 April 2000 event, while of the four other IP shocks examined, only the 24 October 1997 event has $\beta_{\| c} \leq 1.0$ anywhere upstream (for $\sim$24 minutes immediately upstream of the ramp). The low $\beta_{\| c}$ may be a necessary condition for the excitation of shocklets. Recent observations (Wilson et al., preprint, 2009) have found evidence to suggest that the stronger heating of the core electrons at the 6 April 2000 event may have resulted from the microinstabilities of *Matsukiyo and Scholer* [2006]. The instabilities are excited by reflected ions, known to exist upstream of supercritical quasi-perpendicular shocks, interacting with the incident solar wind. Thus the likely supercritical nature of the 6 April 2000 event makes it a prime candidate for these instabilities.

[40] The electron distributions showed a clear relationship between the core/halo temperature anisotropy and shocklets. Regardless of how the halo electrons became anisotropic $T_{\perp h}/T_{\| h}$ downstream of the shocklets, it exceeded the threshold estimated by *Gary et al.* [1994, 1999] for excitation of the whistler heat flux instability. One should also note $T_{\perp h}/T_{\| h}$ increases more dramatically than $T_{\perp c}/T_{\| c}$ across almost every shocklet observed with a leading magnetosonic whistler, consistent with the simulation results of *Gary et al.* [1994, 1999] and *Saito and Gary* [2007]. Thus it appears that the higher-energy halo electrons may have experienced a more efficient pitch angle diffusion than the lower-energy core. Another interesting observation is that nearly every distribution within 30 s of each IP shock ramp exceeded the $T_{\| h}/T_{\| c}$ threshold for whistler heat flux instability estimated by *Gary et al.* [1994].

[41] In addition to particle distributions unstable to the whistler heat flux instability, an electron heat flux was observed. The heat flux itself is the source of the free energy for the instability while the halo electron anisotropies change the threshold and growth rate of the instability. The the heat flux magnitude, angle between wave vector and heat flux, and angle between heat flux vector and magnetic field all peak in the 1631:44–1631:47 UT PAD which is just downstream of the peak amplitude of shocklet B in Figure 2. Also, the angle between the wave vectors and heat flux vectors calculated for each PAD change from $\sim 20^\circ$ to $\sim 27^\circ$ for 1631:32–1631:44 UT. The absolute angle between the magnetic field and heat flux vector changes from $\sim 9^\circ$ to $\sim 24^\circ$ for the same PADs, consistent with the magnetosonic whistler pitch angle scattering the heat flux carrying electrons [*Gary et al.*, 1994].

[42] The PADs downstream of the shocklets are suggestive of perpendicular heating and pitch angle diffusion. However, it is unclear whether the unstable electron distributions seen in the downstream region play any role in the shocklet formation. If the unstable distributions do excite a whistler heat flux instability, the resultant waves could potentially propagate upstream of the steepened edge of the shocklets producing the observed wave train. The waves could prolong or increase the perpendicular electron heating, thus producing more unstable distributions. This would lead to a cyclical behavior of wave formation, propagation, and damping that would be self reinforcing. However, it is also possible that electrons with smaller pitch angles were able to return upstream of the shocklets while the higher pitch angle electrons could not [*Larson et al.*, 1996]. This could also explain the strong parallel anisotropies in the electron PADs observed upstream of the shocklets.

[43] The other four IP shocks discussed herein showed characteristics typical of subcritical to marginally critical quasi-perpendicular shocks [*Farris et al.*, 1993]. They each had precursor whistler waves upstream of the ramp and in the ramp. Almost all the precursor whistlers observed had $20^\circ \leq \theta_{kB} \leq 45^\circ$, consistent with theory [*Gary et al.*, 1994, 1999]. The precursor waves observed in this study actually show more similarities to the ~1 Hz whistlers of *Hoppe et al.* [1982] and *Sentman et al.* [1983]. The waves are far more oblique than the previous observations of precursors at IP shocks observed by *Russell et al.* [1983] or the upstream whistlers at IP shocks observed by *Tsurutani et al.* [1983]. More than 90% of the waves had $29^\circ \leq \theta_{kn} \leq 75^\circ$, thus it is not likely that they are phase standing. The waves are also seen in association with anisotropic electron distributions, though less oblique than previous observations of whistlers associated with anisotropic electrons [*Sentman et al.*, 1983]. We found that the anisotropic electron distributions exceed the thresholds for the whistler heat flux instability estimated by *Gary et al.* [1994, 1999]. The threshold conditions for a whistler heat flux instability [*Gary et al.*, 1994, 1999] are met by almost all electron distributions within 30 s of every IP shock in this study.

[44] This is the first study of IP shocks showing the existence of shocklets upstream of a quasi-perpendicular IP shock. To the best of our knowledge, this is also the first study to show evidence of electron distributions that are unstable to an anisotropy and/or heat flux instability in association with observed whistler waves at quasi-perpendicular IP shocks. The simultaneous observation of whistler waves and anisotropic halo electrons near every shock examined supports the conclusions of *Gary et al.* [1994, 1999] suggesting that halo electrons are more important for the excitation of whistler waves than the core. This also suggests that the anisotropies often observed in the ambient solar wind halo electron distributions may be more unstable than previous estimates which used the entire distribution to estimate $T_\perp/T_\parallel$. Further examination of IP shocks may yield more observations of shocklets and explain their generation mechanisms. Future studies will examine waveform captures in association with the shocklets observed here as possible energy dissipation sources for the shocklets.

Appendix A: Distribution Tests

[45] We performed two tests to determine the stability of our original estimates and to observe the effects on our comparisons to the instability estimates of *Gary et al.* [1994, 1999]. The first test was to lower and raise our cutoff energy bin for the minimum energy of the halo electrons to raise and lower our estimate of n_{he}/n_e. Occasionally our estimates of n_{he}/n_e were a factor of 5–10 less (for the 10 December 1997 and 6 April 2000 events) than the estimate used by *Gary et al.* [1994], $n_{he}/n_e = 0.05$. The second test was a rigorous examination of our fit estimates which we compare to the anisotropy estimates calculated directly from the 3DP particle data. Note, since *Gary et al.* [1999] explicitly removed the strahl electrons from their calculations, we ignored the component of the strahl electrons and only fit to the more isotropic halo components.

[46] The results of the first test showed the largest relative change in the relevant parameters of *Gary et al.* [1994, 1999] occurred in $\beta_{\parallel c}$ and $T_{\parallel h}/T_{\parallel c}$. When we lowered(raised) the cutoff energy, both $\beta_{\parallel c}$ and $T_{\parallel h}/T_{\parallel c}$ decreased(increased). However, for most distributions $T_{\perp h}/T_{\parallel h}$ increased(decreased). Since $T_{\perp h}/T_{\parallel h}$ changed inversely with respect to $T_{\parallel h}/T_{\parallel c}$, we concluded that changing the energy bins did not dramatically affect the instability estimates. Almost all of the PADs which were unstable in our original estimates were still unstable after lowering the lowest energy of the halo electrons. In fact, many of the PADs for the four IP shocks without shocklets were more unstable when we lowered the energy cutoff. For both estimates of break energies, almost all the distributions within 30 s of all five IP shock ramps were unstable to the whistler heat flux instability estimated by *Gary et al.* [1994].

[47] The results of the second test almost always showed a stronger anisotropy in the core and halo electrons than the direct calculations from the data. We found that the strahl electrons, found almost entirely in the parallel component of the electron distribution, lowered estimates of $T_\perp/T_\parallel$ for both the core and halo. The effect is seen more strongly in the halo electrons and *Gary et al.* [1994, 1999] suggested the halo is more important for the whistler heat flux and anisotropy instabilities than the core. This implies that the electron distributions we present may be more unstable than our estimates. Therefore, we used our moment calculations as a lower bound on the halo/core temperature anisotropies.

[48] **Acknowledgments.** We thank R. Lin (3DP), K. Ogilvie (SWE), and R. Lepping (MFI) for the use of data from their instruments. We would also like to thank M. Pulupa, S. D. Bale, P. Schroeder, and M. Wilber for technical help with the 3DP software and analysis. This research was supported by NESSF grant NNX07AU72H and grant NNX07AI05G.

[49] Zuyin Pu thanks the reviewers for their assistance in evaluating this paper.

References

Bougeret, J.-L., et al. (1995), Waves: The radio and plasma wave investigation on the Wind apacecraft, *Space Sci. Rev.*, *71*, 231–263, doi:10.1007/BF00751331.

Fairfield, D. H. (1974), Whistler waves observed upstream from collisionless shocks, *J. Geophys. Res.*, *79*, 1368–1378, doi:10.1029/JA079i010p01368.

Farris, M. H., C. T. Russell, and M. F. Thomsen (1993), Magnetic structure of the low beta, quasi-perpendicular shock, *J. Geophys. Res.*, *98*, 15,285–15,294, doi:10.1029/93JA00958.

Feldman, W. C., J. R. Asbridge, S. J. Bame, M. D. Montgomery, and S. P. Gary (1975), Solar wind electrons, *J. Geophys. Res.*, *80*, 4181–4196, doi:10.1029/JA080i031p04181.

Gary, S. P., E. E. Scime, J. L. Phillips, and W. C. Feldman (1994), The whistler heat flux instability: Threshold conditions in the solar wind, *J. Geophys. Res.*, *99*, 23,391–23,399, doi:10.1029/94JA02067.

Gary, S. P., R. M. Skoug, and W. Daughton (1999), Electron heat flux constraints in the solar wind, *Phys. Plasmas*, *6*, 2607–2612, doi:10.1063/1.873532.

Hada, T., C. F. Kennel, and T. Terasawa (1987), Excitation of compressional waves and the formation of shocklets in the Earth's foreshock, *J. Geophys. Res.*, *92*, 4423–4435, doi:10.1029/JA092iA05p04423.

Hoppe, M. M., and C. T. Russell (1983), Plasma rest frame frequencies and polarizations of the low-frequency upstream waves: ISEE 1 and 2 observations, *J. Geophys. Res.*, *88*, 2021–2027, doi:10.1029/JA088iA03p02021.

Hoppe, M. M., C. T. Russell, L. A. Frank, T. E. Eastman, and E. W. Greenstadt (1981), Upstream hydromagnetic waves and their association with backstreaming ion populations: ISEE 1 and 2 observations, *J. Geophys. Res.*, *86*, 4471–4492, doi:10.1029/JA086iA06p04471.

Hoppe, M. M., C. T. Russell, T. E. Eastman, and L. A. Frank (1982), Characteristics of the ULF waves associated with upstream ion beams, *J. Geophys. Res.*, *87*, 643–650, doi:10.1029/JA087iA02p00643.

Khrabrov, A. V., and B. U. Ö. Sonnerup (1998), Error estimates for minimum variance analysis, *J. Geophys. Res.*, *103*, 6641–6652, doi:10.1029/97JA03731.

Larson, D. E., et al. (1996), Probing the Earth's bow shock with upstream electrons, *Geophys. Res. Lett.*, *23*, 2203–2206, doi:10.1029/96GL02382.

Le, G., C. T. Russell, and E. J. Smith (1989), Discrete wave packets upstream from the Earth and comets, *J. Geophys. Res.*, *94*, 3755–3760, doi:10.1029/JA094iA04p03755.

Lepping, R. P., et al. (1995), The Wind magnetic field investigation, *Space Sci. Rev.*, *71*, 207–229, doi:10.1007/BF00751330.

Lin, R. P., et al. (1995), A three-dimensional plasma and energetic particle investigation for the Wind spacecraft, *Space Sci. Rev.*, *71*, 125–153, doi:10.1007/BF00751328.

Lucek, E. A., and A. Balogh (1997), Ulysses observations of a discrete wavepacket upstream of an interplanetary shock, *Geophys. Res. Lett.*, *24*, 2387–2390, doi:10.1029/97GL52471.

Lucek, E. A., T. S. Horbury, M. W. Dunlop, P. J. Cargill, S. J. Schwartz, A. Balogh, P. Brown, C. Carr, K.-H. Fornacon, and E. Georgescu (2002), Cluster magnetic field observations at a quasi-parallel bow shock, *Ann. Geophys.*, *20*, 1699–1710.

Matsukiyo, S., and M. Scholer (2006), On microinstabilities in the foot of high Mach number perpendicular shocks, *J. Geophys. Res.*, *111*, A06104, doi:10.1029/2005JA011409.

Mellott, M. M., and E. W. Greenstadt (1984), The structure of oblique subcritical bow shocks: ISEE 1 and 2 observations, *J. Geophys. Res.*, *89*, 2151–2161, doi:10.1029/JA089iA04p02151.

Meziane, K., and C. D'Uston (1998), A statistical study of the upstream intermediate ion boundary in the Earth's foreshock, *Ann. Geophys.*, *16*, 125–133, doi:10.1007/s005850050585.

Meziane, K., et al. (2004), Simultaneous observations of field-aligned beams and gyrating ions in the terrestrial foreshock, *J. Geophys. Res.*, *109*, A05107, doi:10.1029/2003JA010374.

Omidi, N., and D. Winske (1990), Steepening of kinetic magnetosonic waves into shocklets: Simulations and consequences for planetary shocks and comets, *J. Geophys. Res.*, *95*, 2281–2300, doi:10.1029/JA095iA03p02281.

Paschmann, G., N. Sckopke, I. Papamastorakis, J. R. Asbridge, S. J. Bame, and J. T. Gosling (1981), Characteristics of reflected and diffuse ions upstream from the Earth's bow shock, *J. Geophys. Res.*, *86*, 4355–4364, doi:10.1029/JA086iA06p04355.

Russell, C. T., D. D. Childers, and P. J. Coleman Jr. (1971), OGO 5 observations of upstream waves in the interplanetary medium: Discrete wave packets, *J. Geophys. Res.*, *76*, 845–861, doi:10.1029/JA076i004p00845.

Russell, C. T., E. J. Smith, B. T. Tsurutani, J. T. Gosling, and S. J. Bame (1983), Multiple spacecraft observations of interplanetary shocks: Characteristics of the upstream ULF turbulence, *NASA Conf. Publ.*, *228*, 385–400.

Saito, S., and S. P. Gary (2007), Whistler scattering of suprathermal electrons in the solar wind: Particle-in-cell simulations, *J. Geophys. Res.*, *112*, A06116, doi:10.1029/2006JA012216.

Scholer, M. (1993), Upstream waves, shocklets, short large-amplitude magnetic structures and the cyclic behavior of oblique quasi-parallel collisionless shocks, *J. Geophys. Res.*, *98*, 47–57, doi:10.1029/92JA01875.

Scholer, M., and J. W. Belcher (1971), The effect of Alfvén waves on MHD fast shocks, *Sol. Phys.*, *16*, 472–483, doi:10.1007/BF00162490.

Scholer, M., H. Kucharek, and I. Shinohara (2003), Short large-amplitude magnetic structures and whistler wave precursors in a full-particle quasi-parallel shock simulation, *J. Geophys. Res.*, *108*(A7), 1273, doi:10.1029/2002JA009820.

Schwartz, S. J., D. Burgess, W. P. Wilkinson, R. L. Kessel, M. Dunlop, and H. Luehr (1992), Observations of short large-amplitude magnetic structures at a quasi-parallel shock, *J. Geophys. Res.*, *97*, 4209–4227, doi:10.1029/91JA02581.

Sentman, D. D., M. M. Hoppe, M. F. Thomsen, S. P. Gary, and W. C. Feldman (1983), The oblique whistler instability in the Earth's foreshock, *J. Geophys. Res.*, *88*, 2048–2056, doi:10.1029/JA088iA03p02048.

Stasiewicz, K., M. Longmore, S. Buchert, P. K. Shukla, B. Lavraud, and J. Pickett (2003), Properties of fast magnetosonic shocklets at the bow shock, *Geophys. Res. Lett.*, *30*(24), 2241, doi:10.1029/2003GL017971.

Thomsen, M. F., S. P. Gary, W. C. Feldman, T. E. Cole, and H. C. Barr (1983a), Stability of electron distributions within the Earth's bow shock, *J. Geophys. Res.*, *88*, 3035–3045, doi:10.1029/JA088iA04p03035.

Thomsen, M. F., J. T. Gosling, and S. J. Schwartz (1983b), Observational evidence on the origin of ions upstream of the Earth's bow shock, *J. Geophys. Res.*, *88*, 7843–7852, doi:10.1029/JA088iA10p07843.

Thomsen, M. F., J. T. Gosling, S. J. Bame, and M. M. Mellott (1985), Ion and electron heating at collisionless shocks near the critical Mach number, *J. Geophys. Res.*, *90*, 137–148, doi:10.1029/JA090iA01p00137.

Tokar, R. L., D. A. Gurnett, and W. C. Feldman (1984), Whistler mode turbulence generated by electron beams in Earth's bow shock, *J. Geophys. Res.*, *89*, 105–114, doi:10.1029/JA089iA01p00105.

Tsubouchi, K., and B. Lembège (2004), Full particle simulations of short large-amplitude magnetic structures (SLAMS) in quasi-parallel shocks, *J. Geophys. Res.*, *109*, A02114, doi:10.1029/2003JA010014.

Tsurutani, B. T., E. J. Smith, and D. E. Jones (1983), Waves observed upstream of interplanetary shocks, *J. Geophys. Res.*, *88*, 5645–5656, doi:10.1029/JA088iA07p05645.

C. A. Cattell, K. Goetz, P. J. Kellogg, K. Kersten, and L. B. Wilson III, Department of Physics and Astronomy, University of Minnesota, 116 Church Street SE, Minneapolis, MN 55455, USA. (cattell@fields.space.umn.edu; goetz@umn.edu; pauljkellogg@gmail.com; kkersten@physics.umn.edu; wilson@physics.umn.edu)

J. C. Kasper, Harvard-Smithsonian Center for Astrophysics, Harvard University, Perkins 138, MS 58, 60 Garden Street, Cambridge, MA 02138, USA. (jkasper@cfa.harvard.edu)

K. Meziane, Physics Department, University of New Brunswick, P.O. Box 4400, 8 Bailey Drive, Fredericton, NB E3B 5A3, Canada. (karim@unb.ca)

A. Szabo, NASA Goddard Space Flight Center, Building 21, Room 156, Greenbelt, MD 20771, USA. (adam.szabo-1@nasa.gov)